Solitary waves in bistable lattices with stiffness grading: Augmenting propagation control

Myungwon Hwang and Andres F. Arrieta*
School of Mechanical Engineering, Purdue University, West Lafayette, Indiana 47907, USA

(Received 16 June 2018; published 4 October 2018)

In this study we introduce small perturbations in the forms of graded intersite stiffnesses and graded on-site potentials to a lattice composed of bistable unit cells under elastic interactions. Based on a known soliton solution in the ϕ-4 model, we use a perturbation approach to approximate the effects of the perturbations on the propagation speeds of transition waves. Numerical validations follow on the exact discrete equations of motion, from which we observe eventual stoppage of transition waves in the periodic lattice under physical damping, unidirectional propagation of the waves in the direction of softening properties, and boomerang-like reflection of the waves in the stiffening direction. Finally, we present three-dimensional-printed experimental lattices, confirming the theoretical and numerical results. The observed behaviors imply the extreme controllability of solitary waves through slight engineering manipulations in material-level structures. We further find that both kink (rarefaction) and antikink (compression) waves are allowed at any site in the lattice, extending the functionality of the lattice in engineering applications such as energy harvesting.

DOI: 10.1103/PhysRevE.98.042205

I. INTRODUCTION

The utilization of nonlinearities in lattice systems has been the focus of substantial research due to its potential to generate classes of solitary waves [1–3], which are large-amplitude, spatially localized waves exhibiting more robust transport properties than their linear counterparts. In the context of uniform periodic lattices, a considerable amount of theoretical and numerical groundwork has been laid for the dynamics and formations of such nonlinear waves, encompassing topological solitons, nontopological solitons, envelope solitons, and breathers [4–14]. To bridge the gap between the idealization and physical reality, where no materials are perfect, and thus the effects of relaxed periodicity on the solitary waves are of physical importance, a series of studies on perturbed systems have followed. In particular, inhomogeneities in the forms of external force, boundaries, dissipation, substrate or mass impurities, and stochastic or harmonic variations in additive and/or multiplicative terms have been extensively analyzed in both sine-Gordon [15–19] and ϕ-4 [20–23] models. However, the dynamics of lattices supporting strongly nonlinear waves under the presence of graded properties have not received much attention.

In spite of the well-established theoretical and numerical studies on solitary waves, their experimental manifestations are still rare. The major experimental advances have been made in the observations and utilizations of nontopological solitary waves arising from the strong Hertzian contact forces in granular chains [24–32]. However, the experimental demonstration of topological solitary waves had long been limited to the classical pendula model [33]. Recently, stable propagation of topological solitary waves, or state transition waves, has been successfully demonstrated in a chain of repelling magnets [34] and in a periodic lattice formed by bistable unit cells [35,36] under magnetic interactions [37]. The latter results in extreme unidirectional wave guiding, and it has been further observed that its response is independent of the type and intensity of the input excitations, which suggests its potential implementation for broadband energy harvesting and protective metamaterials [38]. In an elastically connected periodic bistable lattice made of highly dissipative soft media, Raney *et al.* [39] have also demonstrated similar transition waves for high-fidelity, controllable signal transmission. For uninterrupted propagation of transition waves, both types of bistable lattices in the previous studies utilize the stored energy between asymmetric on-site potential wells in periodic arrangements to balance out the inherent dissipation. This choice destroys one of the two soliton solutions (kink and antikink), limiting their functionalities in that no intrinsic repositioning mechanism is available.

In this paper, we study the dynamics of lattices of symmetric bistable elements exhibiting spatially varying properties, investigating the effects of the grading on the propagation characteristics of transition waves. To that end, we begin with linear perturbation from the known soliton solutions of the ϕ-4 model to find the approximate propagation speeds of the solitons for each case. The numerical simulations on the exact equations of motion follow to validate the theoretical predictions, and finally, we present three-dimensional (3D) -printed lattice samples demonstrating all of the predicted behaviors in physical settings. We show that the introduction of spatial grading allows for this class of lattices to support compression and rarefaction topological solitons in contrast to periodic arrangements, thereby providing an intrinsic mechanism for resetting the states of all the elements in the arrangement. The existence of the two possible topological soliton solutions allows for the exciting nonlinear dynamics of bistable lattices to be exploited in important applications, such as energy harvesting or soft robotics.

*aarrieta@purdue.edu

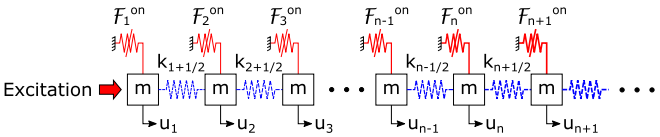

FIG. 1. A schematic representation of the bistable lattice with elastic intersite interactions. A unit cell is composed of a mass and an on-site bistable element (in solid red), and each unit cell is coupled with the neighboring cell by intersite linear springs (in dashed blue). Both the intersite and on-site elements are allowed to vary in stiffness.

II. LATTICE DESCRIPTION

A simple one-dimensional chain of a spring-mass system is used to represent the lattice model. Each unit cell is composed of a bistable element (depicted by solid red lines in Fig. 1) with a mass that is connected to the nearest neighbors by linear springs (dashed blue lines in Fig. 1). The governing equation of motion can be written as

$$m u_{n,tt} = k_{n+\frac{1}{2}}(u_{n+1} - u_n) - k_{n-\frac{1}{2}}(u_n - u_{n-1}) + \mathcal{F}_n^{\text{on}}(u_n) - d u_{n,t}\,, \tag{1}$$

where u_n and $\mathcal{F}_n^{\text{on}}$ represent the displacement and on-site force of the nth element, and $k_{n-\frac{1}{2}}$ and $k_{n+\frac{1}{2}}$ are the spring stiffness to the left and right of the element. The mass m and on-site damping d remain invariant through the lattice. The masses are separated from one another by a constant lattice spacing L, although it does not explicitly appear in the equation.

For a more compact mathematical treatment, the governing equation is nondimensionalized to

$$\bar{u}_{n,\bar{t}\bar{t}} = \bar{k}_{n+\frac{1}{2}}(\bar{u}_{n+1} - \bar{u}_n) - \bar{k}_{n-\frac{1}{2}}(\bar{u}_n - \bar{u}_{n-1}) + \bar{\mathcal{F}}_n^{\text{on}}(\bar{u}_n) - \bar{d}\,\bar{u}_{n,\bar{t}}\,, \tag{2}$$

where the following nondimensionalization is used:

$$u_n = L\bar{u}_n, \quad t = \tau\bar{t}, \quad \tau = \sqrt{\frac{m}{k_1}}, \qquad \bar{k}_n = \frac{k_n}{k_1}, \quad \bar{d} = \frac{d}{m}\tau, \quad \bar{\mathcal{F}}_n^{\text{on}} = \frac{\mathcal{F}_n^{\text{on}}}{k_1 L}. \tag{3}$$

This discrete equation is in general difficult to solve exactly, and thus we seek a continuum-limit model for an approximate solution. Expanding $\bar{u}_{n\pm1}(\bar{t}) = \bar{u}(\bar{x}\pm1,\bar{t}) = \bar{u}(\bar{x},\bar{t}) \pm \frac{\partial\bar{u}(\bar{x},\bar{t})}{\partial\bar{x}} + \frac{1}{2}\frac{\partial^2\bar{u}(\bar{x},\bar{t})}{\partial\bar{x}^2}$, $\bar{k}_{n\pm\frac{1}{2}} = \bar{k}(\bar{x}\pm\frac{1}{2}) = \bar{k}(\bar{x}) \pm \frac{1}{2}\frac{\partial\bar{k}}{\partial\bar{x}} + \frac{1}{8}\frac{\partial^2\bar{k}}{\partial\bar{x}^2}$ and letting L approach 0, we obtain

$$\frac{\partial^2\bar{u}(\bar{x},\bar{t})}{\partial\bar{t}^2} - \bar{k}(\bar{x})\frac{\partial^2\bar{u}(\bar{x},\bar{t})}{\partial\bar{x}^2} - \frac{\partial\bar{k}(\bar{x})}{\partial\bar{x}}\frac{\partial\bar{u}(\bar{x},\bar{t})}{\partial\bar{x}} - \bar{\mathcal{F}}^{\text{on}}(\bar{u},\bar{x}) + \bar{d}\frac{\partial\bar{u}(\bar{x},\bar{t})}{\partial\bar{t}} = 0. \tag{4}$$

The on-site force $\bar{\mathcal{F}}^{\text{on}}(\bar{u},\bar{x})$ should represent bistability of each unit cell, providing a necessary condition for the generation of transition waves. The lowest polynomial that can represent the bistability of the on-site force is a cubic function (referred to as a ϕ-4 potential in most literature); one such expression for a symmetric on-site potential is $\omega_0^2(\bar{u} - \bar{u}^3/u_0^2)$, where ω_0 and u_0 are arbitrary constants. By letting $a(\bar{x})$ and $b(\bar{x})$ be small perturbations from the reference stiffness $\bar{k}_1$ and the reference on-site force $\bar{\mathcal{F}}^{\text{on}}(\bar{u},0)$ such that $\bar{k}(\bar{x}) = 1 + a(\bar{x})$ and $\bar{\mathcal{F}}^{\text{on}}(\bar{u},\bar{x}) = [1 + b(\bar{x})]\omega_0^2(\bar{u} - \bar{u}^3/u_0^2)$, respectively, the final equation can be written without loss of generality as

$$\frac{\partial^2\bar{u}}{\partial\bar{t}^2} - [1 + a(\bar{x})]\frac{\partial^2\bar{u}}{\partial\bar{x}^2} - \frac{\partial a(\bar{x})}{\partial\bar{x}}\frac{\partial\bar{u}}{\partial\bar{x}} - [1 + b(\bar{x})]\omega_0^2\big(\bar{u} - \bar{u}^3/u_0^2\big) + \bar{d}\frac{\partial\bar{u}}{\partial\bar{t}} = 0. \tag{5}$$

By setting $X = \omega_0\bar{x}$, $T = \omega_0\bar{t}$, $\bar{u} = u_0 F$, $a(\bar{x}) = \alpha(X)$, $b(\bar{x}) = \beta(X)$, and $\bar{d} = \omega_0\delta$, Eq. (5) can further be reduced into a canonical form:

$$F_{,TT} - [1 + \alpha(X)]F_{,XX} - \alpha'(X)F_{,X} + [1 + \beta(X)](F^3 - F) + \delta F_{,T} = 0. \tag{6}$$

III. THEORETICAL ANALYSES

The exact solution to Eq. (6) is not known, and so we seek a perturbed solution from a known soliton solution in the periodic lattice without any perturbations: $\alpha(X), \beta(X), \delta = 0$. Applying a Lorentz transformation,

$$\xi = \gamma(X - vT), \quad \tau = \gamma(T - vX), \quad \gamma = \frac{1}{\sqrt{1 - v^2}}, \qquad X = \gamma(\xi + v\tau), \quad T = \gamma(\tau + v\xi), \tag{7}$$

Eq. (6) becomes

$$[1 - \alpha(X)\gamma^2v^2]F_{,\tau\tau} + 2v\alpha(X)\gamma^2F_{,\tau\xi} - [1 + \alpha(X)\gamma^2]F_{,\xi\xi} + \gamma[\alpha'(X)v + \delta]F_{,\tau} - \gamma[\alpha'(X) + \delta v]F_{,\xi} + [1 + \beta(X)](F^3 - F) = 0. \tag{8}$$

Since the unperturbed equation is invariant under Lorentz transformation and the velocity v is a free parameter, we can work with a static soliton in a moving frame traveling to the $+\xi$ direction (to the right) with v. In the physical frame, the soliton itself can be considered to travel to the right.

Assuming a perturbed solution $F(\xi,\tau) = F_s(\xi,\tau) + f(\xi,\tau)$, where $F_s(\xi,\tau)$ is the soliton solution of the equation

$$F_{s,\tau\tau} - F_{s,\xi\xi} + F_s^3 - F_s = 0, \tag{9}$$

Eq. (8) becomes

$$[1 - \alpha(X)\gamma^2v^2](F_{s,\tau\tau} + f_{,\tau\tau}) + 2v\alpha(X)\gamma^2(F_{s,\tau\xi} + f_{,\tau\xi}) - [1 + \alpha(X)\gamma^2](F_{s,\xi\xi} + f_{,\xi\xi}) + \gamma[\alpha'(X)v + \delta](F_{s,\tau} + f_{,\tau}) - \gamma[\alpha'(X) + \delta v](F_{s,\xi} + f_{,\xi}) + [1 + \beta(X)]\big(F_s^3 + 3F_s^2 f + 3F_s f^2 + f^3 - F_s - f\big) = 0. \tag{10}$$

Subtracting the unperturbed equation of motion [Eq. (9)] from Eq. (10) and substituting the known solution $F_s(\xi,\tau)=\tanh\frac{\xi}{\sqrt{2}}$ (kink soliton), we obtain

$$\begin{aligned}&[1-\alpha(X)\gamma^2v^2]f_{,\tau\tau}+2v\alpha(X)\gamma^2f_{,\tau\xi}-[1+\alpha(X)\gamma^2]f_{,\xi\xi}+\gamma[\alpha'(X)v+\delta]f_{,\tau}-\gamma[\alpha'(X)+\delta v]f_{,\xi}\\&+[1+\beta(X)]\left(2-3\,\mathrm{sech}^2\frac{\xi}{\sqrt{2}}\right)f+\alpha(X)\gamma^2\,\mathrm{sech}^2\frac{\xi}{\sqrt{2}}\tanh\frac{\xi}{\sqrt{2}}\\&-\frac{1}{\sqrt{2}}\gamma[\alpha'(X)+\delta v]\,\mathrm{sech}^2\frac{\xi}{\sqrt{2}}-\beta(X)\,\mathrm{sech}^2\frac{\xi}{\sqrt{2}}\tanh\frac{\xi}{\sqrt{2}}=0,\end{aligned}\tag{11}$$

where only up to the linear terms of the small perturbation $f(\xi,\tau)$ are retained. Note that $F_{s,\tau}=F_{s,\tau\tau}=0$ since the selected soliton solution is static in the transformed coordinate.

The ϕ-4 soliton has a known set of two bound states (ψ_b and ψ_1) and scattering states (ψ_k), which form a complete set [3]. Therefore,

$$f(\xi,\tau)=\frac{1}{c_b}\phi_b(\tau)\psi_b(\xi)+\frac{1}{c_1}\phi_1(\tau)\psi_1(\xi)+\int\phi_k(\tau)\psi_k(\xi)\,dk,\tag{12}$$

where

$$\begin{aligned}&\int_{-\infty}^{+\infty}d\xi\;\psi_b^*(\xi)\psi_b(\xi)=\frac{1}{2}\int_{-\infty}^{+\infty}d\xi\;\mathrm{sech}^4\frac{\xi}{\sqrt{2}}=c_b,\\&\int_{-\infty}^{+\infty}d\xi\;\psi_1^*(\xi)\psi_1(\xi)=\frac{1}{2^{3/2}}\int_{-\infty}^{+\infty}d\xi\;\tanh^2\frac{\xi}{\sqrt{2}}\,\mathrm{sech}^2\frac{\xi}{\sqrt{2}}=c_1,\\&\int_{-\infty}^{+\infty}d\xi\;\psi_k^*(\xi)\psi_{k'}(\xi)=\underbrace{\delta(k-k')}_{\text{dirac delta function}}.\end{aligned}\tag{13}$$

Since we are interested in the translation mode ψ_b of the soliton, we project Eq. (11) onto ϕ_b, the details of which are provided in Supplemental Material [40]. Assuming linear [$\alpha(X)=\tilde{\alpha}X$, $\beta(X)=\tilde{\beta}X$] and small ($\tilde{\alpha},\tilde{\beta}\ll1$) variations in the perturbations, low propagation speed ($v\ll1$), and weak coupling between different modes for a qualitative analysis, Eq. (11) becomes

$$\phi_{b,\tau\tau}+\gamma\delta\phi_{b,\tau}=-\tfrac{1}{2}\gamma^3\tilde{\alpha}c_b+\gamma\tilde{\alpha}c_b+\gamma\delta vc_b+\tfrac{1}{2}\gamma\tilde{\beta}c_b.\tag{14}$$

This is a second-order ordinary differential equation, and its solution yields

$$\phi_b(\tau)=\frac{c_b[(2-\gamma^2)\tilde{\alpha}+\tilde{\beta}+2v\delta]}{2\delta}\left[\tau+\frac{e^{-\gamma\delta\tau}-1}{\gamma\delta}\right].\tag{15}$$

Since $\phi_b(\tau)/c_b$ is the coefficient of the translating mode $\psi_b(\xi)$, its increase represents movement to the left in the spatial coordinate ξ. The presented analyses above are performed in a moving frame, implying that the actual physical velocity corresponds to $v-\phi_b'(\tau)/c_b$, which asymptotically approaches

$$v_{\text{prop}}\to v-\frac{(2-\gamma^2)\tilde{\alpha}+\tilde{\beta}+2v\delta}{2\delta}.\tag{16}$$

The propagation speeds of the soliton due to intersite stiffness changes from this approximate relation are plotted in Fig. 2(a). When there is damping only ($\delta=1$), the propagation speed approaches zero, becoming a static soliton. This result is physically reasonable since there are no other sources providing energy to the system to balance out the dissipated energy, thereby resulting in the static soliton solution. With the softening intersite interaction ($\tilde{\alpha}<0$), the propagation speed always stays positive, indicating that the soliton can travel an arbitrary distance without ever stopping. This can be an alternative method to attain a unidirectional wave propagation. With the stiffening intersite interaction, on the other hand, the soliton slows down to zero, eventually changes the direction of propagation, and continues to travel in the opposite direction. Similarly, Fig. 2(b) shows the propagation speed variations due to the on-site stiffness changes. They have identical trends to those of the intersite stiffness changes: a decreasing stiffness leads to a continued propagation of a soliton, and an increasing stiffness leads to a returning wave.

The obtained results are also valid for the other (antikink) soliton solution $F_s(\xi,\tau)=-\tanh\frac{\xi}{\sqrt{2}}$. Any of the polarity changes in Eq. (11) from using the antikink solution will be recovered upon the projection on the first bound mode ψ_b so that the final differential equation and its solution will be identical to those of the kink soliton case. Thus, a series of alternating compression and rarefaction waves can be continuously triggered anywhere in this bistable lattice model, which is a limitation in the previous studies [37–39]. Therefore, the introduction of spatially graded properties reveals new physical mechanisms for sustaining the unidirectional propagation of solitary waves, as well as for obtaining the two possible topological soliton solutions: rarefaction and compression.

The condition $(2-\gamma^2)\tilde{\alpha}+\tilde{\beta}+2v\delta=0$ appears to reveal that the soliton propagates with a constant speed (two examples are plotted in dashed magenta in Fig. 2); yet care must be taken as the small perturbation assumption no longer holds as τ grows large. The results can be improved by including the coupling terms and computing through an iterative process as described in Dauxois and Peyrard [3]. However, the process requires highly convoluted calculations and lengthy expres-

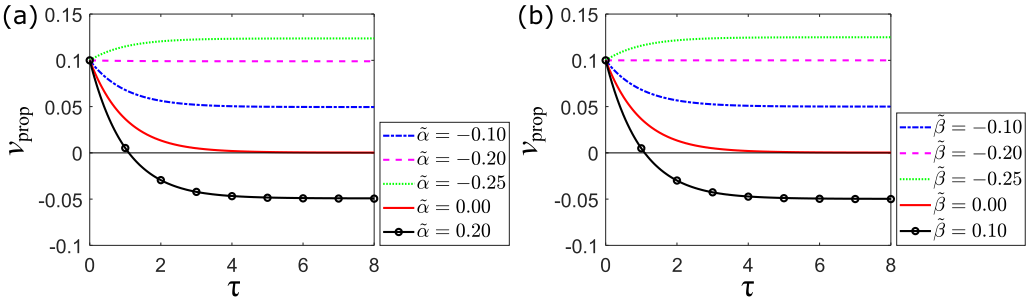

FIG. 2. The theoretical prediction of the propagation speed of the soliton for (a) the intersite stiffness variation $\tilde{\alpha}$ and (b) the on-site stiffness variation $\tilde{\beta}$. The same damping value $\delta = 1$ is used for every plot.

sion. Instead, the qualitative behaviors from this approximate theoretical approach will be validated by the numerical analyses in the following section.

IV. NUMERICAL SIMULATIONS

For the numerical simulations, a central difference method [41] with a constant time step $\Delta\bar{t} = 0.01$ is directly applied to the discrete equation of motion [Eq. (2)]. Linear variations are applied to both intersite stiffness and on-site force changes for simplicity as done in the theoretical analyses, such that $\frac{(\bar{k}_{n+1/2}-\bar{k}_{n-1/2})}{\bar{k}_1}$ and $\frac{(\bar{f}_{n+1}-\bar{f}_n)}{\bar{f}_1}$ are 0.015 for the softening cases and 0.02 for the stiffening cases. A large number of elements ($N = 500$) are used to minimize the response distortion due to the boundary effects. However, only a limited number of elements ($N = 60$) are used for the softening lattices since an arbitrarily long lattice can yield an unphysical negative value for the stiffness. To minimize the discreteness effects, the stiffness ratio between the intersite and on-site members is chosen to be a large value (which ensures gradual displacement changes between the neighboring sites); in this study, the reference intersite stiffness is chosen to be five times higher than the reference on-site stiffness ($\omega_0^2 = 0.1$ and $u_0^2 = 1$). The input excitation is simulated by imposing an initial velocity condition ($d\bar{u}_1/d\bar{t} = \pm 2$) on the first element, and the same on-site damping $\bar{d} = 0.08$ is used throughout the simulations.

Due to the energy dissipation as a wave passes through each element, the triggered transition wave in a periodic bistable lattice is not expected to propagate indefinitely in physical settings. Figure 3(a) shows the time responses at the selected sites and the propagation fronts at several time instants (inset i) in a periodic lattice. The elements between the 18th and 30th sites cease to make complete transitions to the other states, and the wave becomes a stationary soliton after $\bar{t} \approx 60$. In inset ii is the space-time contour of the transition wave, which is numerically obtained by measuring and plotting the time instant that crosses the zero displacement line for each site. The gradient of this contour corresponds to the propagation velocity, confirming that the speed approaches zero in a periodic bistable lattice with damping.

To allow a continued propagation of the transition wave, the total dissipated energy should not exceed the available energy in the lattice. Since the initial excitation energy is fixed and all the on-site potentials are symmetric, no additional energy can be supplied in the course of a wave transmission. One way to achieve the balance is by reducing the mechanical resistance, which is effectively done by continuously softening either the intersite or the on-site stiffnesses. Figure 3(c) shows that the state transition occurs at every investigated site in the bistable lattice with softening intersite stiffnesses. The continued translation of a transition wave in the space configuration at each successive time instant (inset i) reinforces the complete transmission of a transition wave through the lattice. The nonzero propagation speed in inset ii is also in agreement with the theoretically predicted behavior.

A stiffening lattice may be thought of as a flipped version of a softening case. Due to the tendency of the softening lattice to discharge the signal in the softening direction, it is expected that the input signal would return to the excitation point. The time response of each element in the bistable lattice with linearly increasing intersite stiffnesses is plotted in Fig. 3(e). In this case, the first few elements initially jump to the other stable states, but they return to their original states in due course. If seen in the space configuration [inset Fig. 3(e)-i], the main wave front shows a boomerang-like behavior; it initially moves in the direction of the excitation, changes the propagation direction at around site 20, and eventually returns to the excitation site. Again, the characteristic behavior in the space-time contour [inset Fig. 3(e)-ii] agrees with the theoretical result.

The observed transition waves in Figs. 3(a), 3(c), and 3(e) are compressive in nature; however, the theoretical prediction implies that every compression wave is accompanied by a rarefaction wave. Figures 3(b), 3(d), and 3(f) show the propagation of rarefaction waves for each type of the bistable lattices with identical parameters to those for the compression waves except that every on-site element is initially at the other stable state and that the excitation is applied in the opposite direction. It is worth noticing that the excitation is made from the same side of the lattice, enabling signals to be continuously sent from a single input site (site 1 in these examples). Furthermore, the proposed class of graded lattices allows for the rarefaction and compression waves to be triggered from any site on the lattice, remedying the limitation of previously studied periodic lattices. Other than the sign changes, the responses are exactly the same as in the cases with compression waves.

The same qualitative behaviors observed in the bistable lattice with the intersite stiffness variations are present for the on-site stiffness variation as shown in Fig. 4. In the softening direction of the on-site potentials, each successive on-site

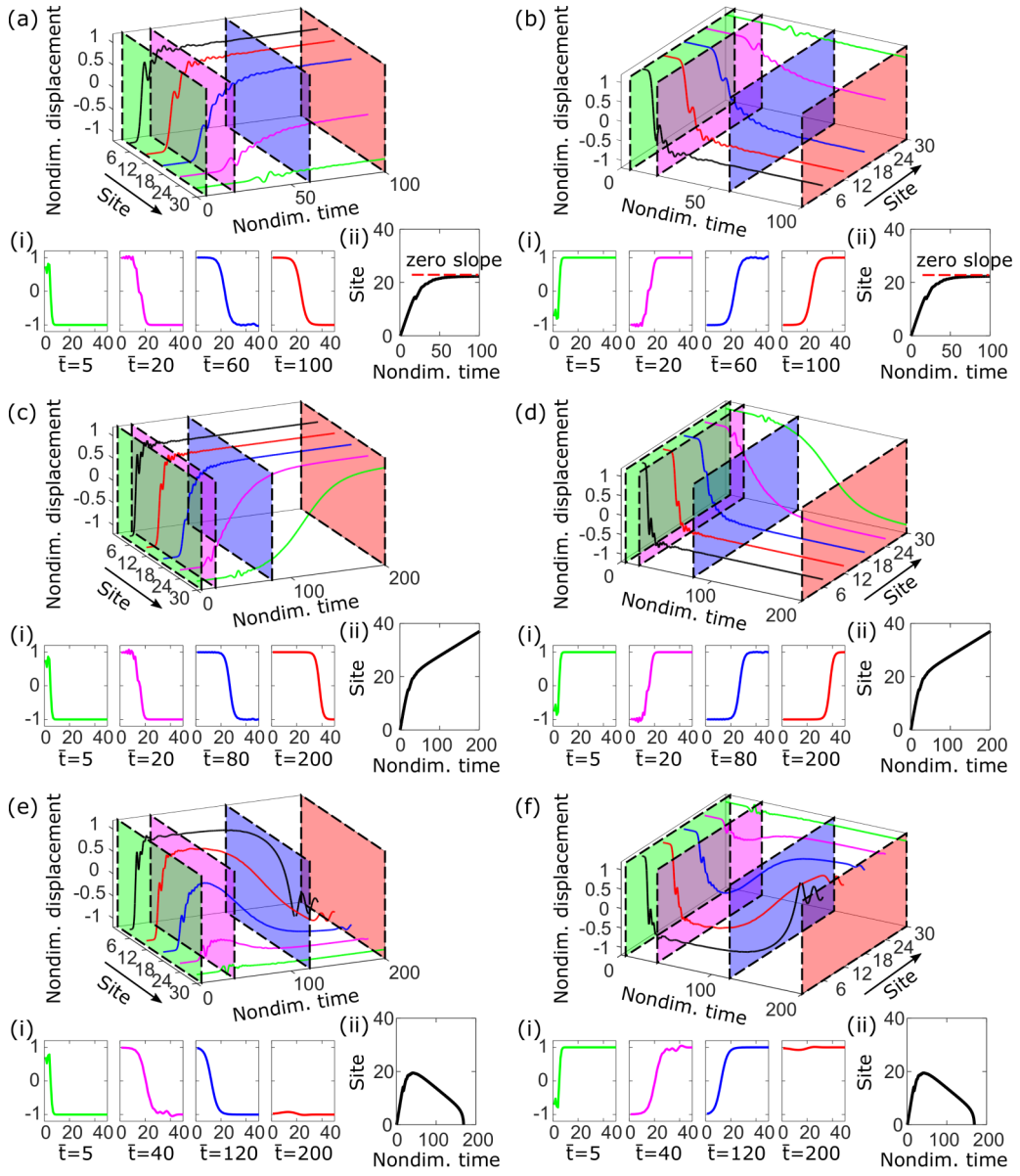

FIG. 3. The propagation of (a) compressive and (b) rarefactional transition waves in the periodic bistable lattice, (c, d) the lattice with linearly decreasing intersite stiffness, and (e, f) the lattice with linearly increasing intersite stiffness. In the inset of each figure are (i) the wave profiles in the space configuration at the selected time instants of interest and (ii) the space-time contour of the transition wave.

element becomes a preferred path, resulting in a complete propagation through the lattice [Figs. 4(a) and 4(b)]. In the stiffening direction, it acts as an increasing barrier, creating a boomerang-like wave transmission that can be observed by the returning of the wave form to the excitation site in insets i and ii of Figs. 4(c) and 4(d). In the sense that the transition wave entering from one side propagates through the lattice, but the one entering from the opposite side does not, the bistable lattice with a monotonic stiffness variation can be viewed as a unidirectional lattice.

V. EXPERIMENTAL VALIDATION

The experimental samples are prepared with a fused-deposition-modeling 3D printer (Ultimaker 3). Two sets of ladder-shaped lattices are 3D-printed and then glued together to form a lattice of 14 unit cells as shown in Fig. 5. A brass ball of diameter 12.7 mm and mass 9.36 g is glued to each web to form a unit cell, and each unit cell is connected to the neighboring elements by spring-shaped features so that they can support both compressive and tensile forces. On the opposite side of the mass attachment, rectangular pieces of black and white speckled patterns are applied to allow for data collection with digital image correlation techniques. The bistabilities of the on-site potentials is achieved by imposing precompression controlled by a universal testing machine (Instron 3345). To collect the experimental dynamic responses, a pair of high-speed cameras (Photron UX100) are used with a frame rate of 2000 fps. The width of the analysis area is focused on the first seven elements from the excitation point to allow for sufficient picture resolution while capturing enough elements to observe the desired behaviors. The collected images are

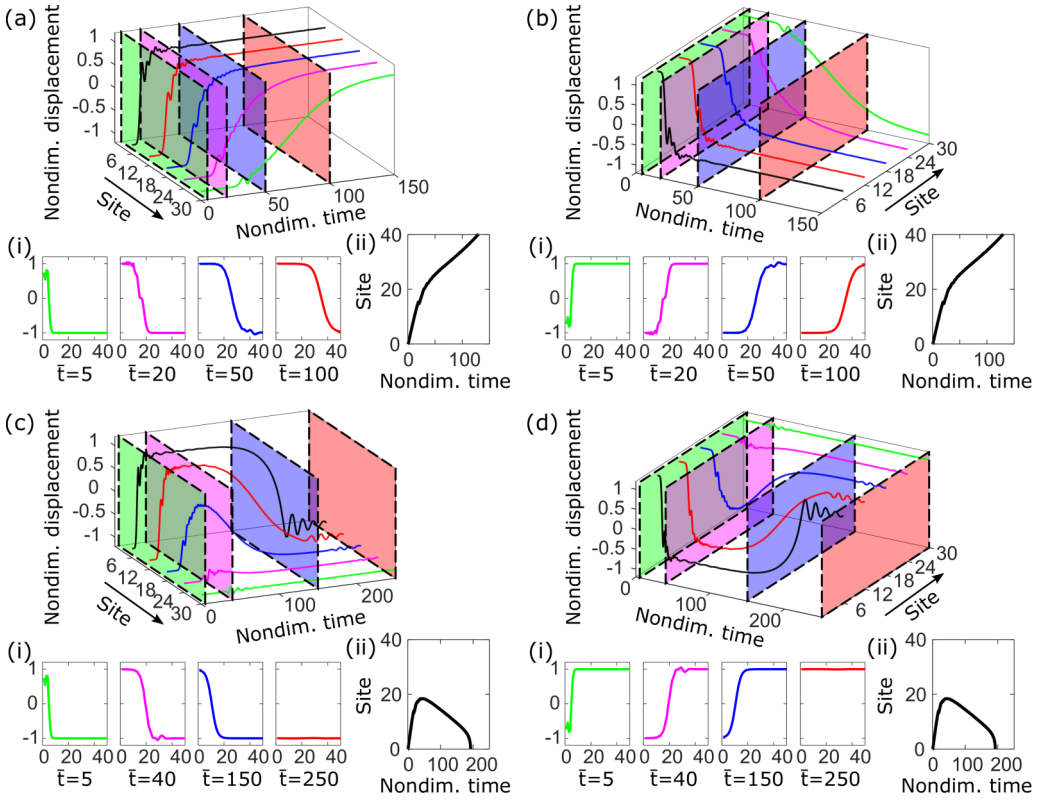

FIG. 4. The propagation of (a) compressive and (b) rarefactional transition waves in the lattice with linearly decreasing on-site stiffness and (c, d) the lattice with linearly increasing on-site stiffness. In the inset of each figure are (i) the wave profiles in the space configuration at the selected time instants of interest and (ii) the space-time contour of the transition wave.

postprocessed using a commercial digital image correlation software (VIC-3D).

Each unit cell is identically designed for the periodic lattice, and 1 mm of precompression is applied, resulting in a snapping distance of about 15 mm between the two stable states. Figure 6(a) shows the time responses of the first seven elements of the periodic lattice from the excitation site (see video S1). The displacements are measured with respect to the initial stable states. It can be observed that the first two elements display complete transitions to the other stable states while the seventh element remains at the same initial state after a transient motion. (The final displacements of the intermediate elements are progressively dispersed between two stable states, which is in line with the gradual variation condition

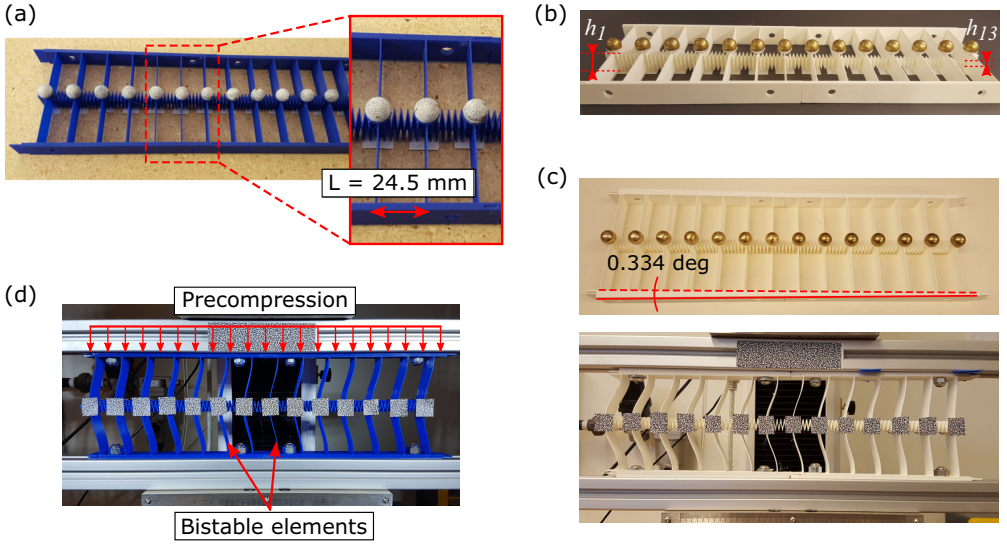

FIG. 5. The 3D-printed samples for (a) the periodic bistable lattice, (b) the bistable lattice with intersite stiffness grading, and (c) the bistable lattice with on-site potential grading. (d) The experimental setup, showing how to create the bistabilities in the on-site members.

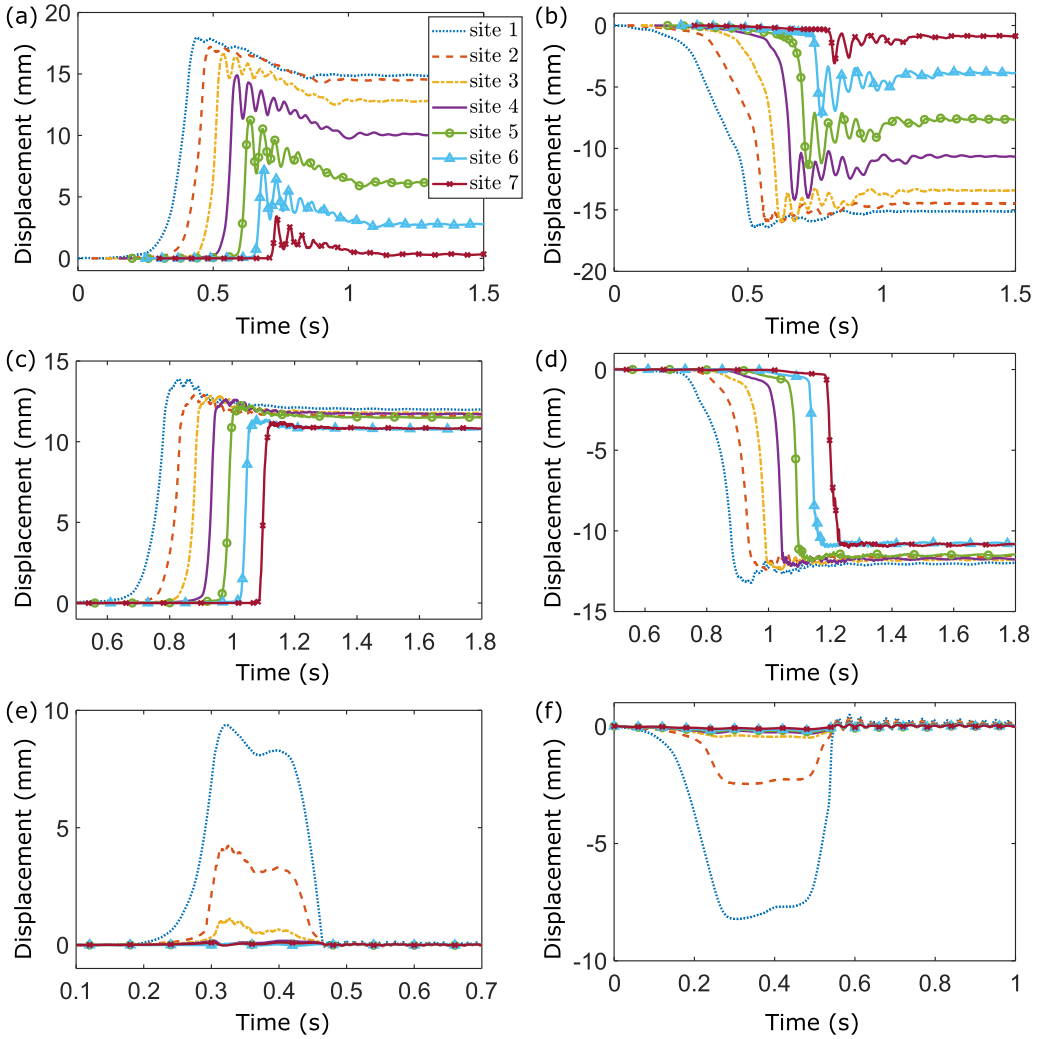

FIG. 6. The time response of the experimental lattices at sites 1–7. The propagation of (a) compression and (b) rarefaction waves in the periodic bistable lattice, (c, d) the lattice with linearly decreasing intersite stiffness, and (e, f) the lattice with linearly increasing intersite stiffness. Each individual displacement in (a–d) is offset in the time axis by 0.05 s for a better presentation of the results.

for the continuum-limit approximation.) This implies that the transition wave does not propagate through the lattice. The observed stabilization as time grows indicates that the transition wave stops inside the lattice, becoming a stationary soliton just as predicted in the theoretical and numerical analyses.

The intersite stiffness variation is controlled by gradually changing the height of the interelement spring elements as shown in Fig. 5(b); the stiffest spring has $h_1 = 17$ mm, and the softest spring has $h_{13} = 5$ mm. For the lattice with linearly decreasing intersite stiffness [Fig. 6(a) and video S2], all of the elements transition into the other stable states, in agreement with the theoretical and numerical predictions. The slight differences in the final displacements after the transition wave passes are due to the imperfections in the test fixtures and the manufacturing variations.

To observe the behavior in the lattice with linearly increasing intersite stiffness, the same lattice as in the decreasing case is used except that now the excitation is made at the opposite end (where the spring stiffness is the softest). In this case, all the analyzed elements return to the initial stable states even though the first element hits the other stable state briefly [Fig. 6(e) and video S3]. The limited manufacturing precision prevents us from showing the more extreme boomerang-like behavior, where the transition wave travels further in the stiffening direction before returning to the excitation point. However, such behavior is physically attainable with the higher ratio between the intersite and on-site stiffness values as can be partially observed in video S4, where the transition wave is triggered at an internal site with a greater intersite stiffness. Figures 6(b), 6(d), and 6(f) show the measured responses of the bistable lattices initially at the second stable states under tensile input excitations. The transmissions of the rarefaction transition waves exhibit the same characteristic behaviors as those of compression waves except the changed polarities and slight deviations in values due to irregularity of the test setup.

The on-site stiffnesses are controlled by applying different precompression levels. This is achieved by designing the flanges with an initial draft angle of 0.334° as shown in Fig. 5(c). Thus, as the two flanges are installed on the parallel test rigs, each individual element is compressed by a differing amount. The precompression is applied in such a way that the softest on-site member is compressed by 0.5 mm and the

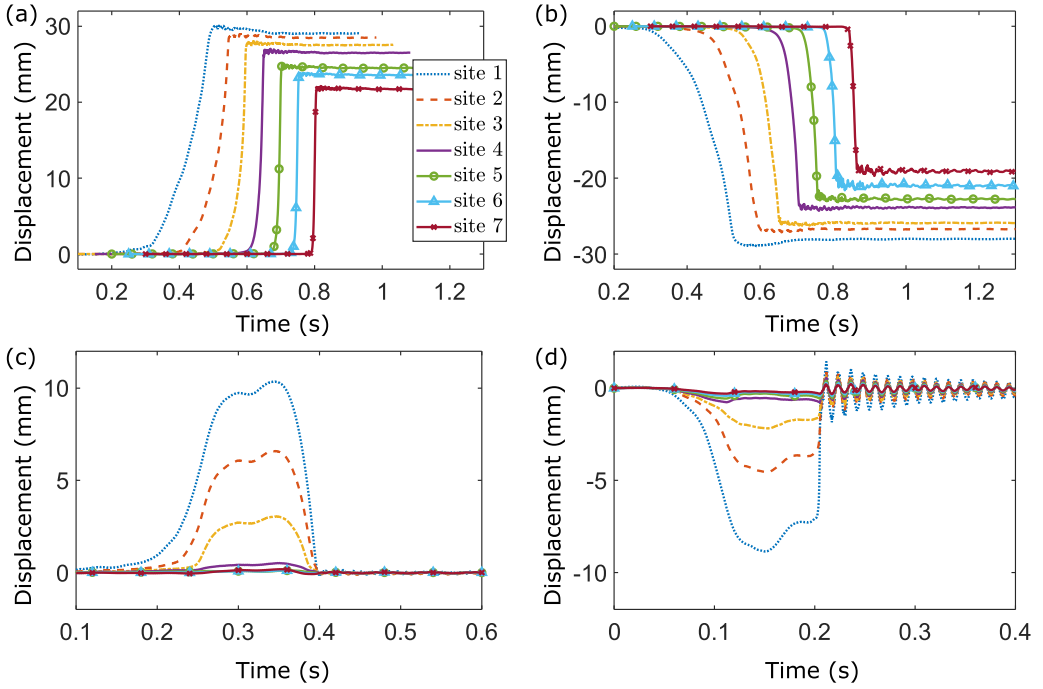

FIG. 7. The time response of the experimental lattices with on-site stiffness grading at sites 1–7. The propagation of (a) compression and (b) rarefaction wave in the lattice with decreasing on-site stiffness and (c, d) the lattice with increasing on-site stiffness. Each individual displacement in (a, b) is offset in the time axis by 0.05 s for a better presentation of the results.

stiffest on-site member by 6 mm. The experimental realization for this case results in the slight deviations from the expected theoretical and numerical observations as the precompression introduces longer snapping distances, which is evident from the different displacements after the state transition occurs at each site in Figs. 7(a) and 7(b). Also, a linear change in compression does not necessarily mean a linear change in the stiffness. However, it is difficult to manufacture linearly varying on-site buckled elements with constant snapping distances with the inherent nonlinear geometry, and thus we opt for qualitative comparison in this study. The overarching effects of having decreasing (increasing) on-site potentials are the same as the effects of decreasing (increasing) intersite stiffnesses, confirming the theoretical and numerical predictions. Figures 7(a) and 7(b) and video S5 show the complete transmission of an antikink and a kink from a single excitation point; Figs. 7(c) and 7(d) and videos S6 and S7 show the reflections of them.

VI. CONCLUSIONS

In this study, we have investigated the effects of introducing spatially graded properties to lattices of bistable elements. Our theoretical analysis predicts that the generated solitary waves cannot propagate completely through the lattice in a physical setting with nonzero damping, using a perturbation method. Rather, these waves become stationary solitons, meaning that the propagation of a transition wave stops inside the lattice. Either linearly decreasing intersite or linearly decreasing on-site stiffnesses enable the continued propagation of transition waves through the lattice even under the presence of strong damping. On the other hand, an interesting boomerang-like transmission of a transition wave is predicted for such lattices with linearly increasing intersite or on-site stiffnesses. These transmission characteristics constitute an alternative way of achieving unidirectionality. A series of numerical simulations and experiments on the 3D-printed bistable lattice samples validate all of our theoretical predictions. The observed behaviors manifest that the directionality of transition waves can be controlled drastically through small manipulations in material-level designs. Furthermore, such architecturing enables the existence of both compression and rarefaction solitons. This allows a simple, yet effective mechanism for creating multifunctional metamaterials with built-in energy harvesting capability owing to the intrinsic resetting mechanism that enables the continued transmission of the transition wave pairs. Further technological applications exploiting the spatial grading of properties are envisioned. For example, a softening arrangement can be used as a robust signal transmission network while the integrated transducer at each unit cell converts energy from the traveling solitary waves. In the stiffening direction, the lattice can act either as a protective material that blocks any transmission of catastrophic inputs or as a phase-delaying mechanism while still manipulating the solitary waves for power conversion.

ACKNOWLEDGMENT

M.H. and A.F.A. gratefully acknowledge the support of the Purdue Research Foundation (PRF); this research was supported through start-up funds provided to A.F.A.

[1] N. J. Zabusky and M. D. Kruskal, Phys. Rev. Lett. **15**, 240 (1965).

[2] M. Remoissenet, *Waves Called Solitons*, 3rd ed., Advanced Texts in Physics (Springer, Berlin, 1999).

[3] T. Dauxois and M. Peyrard, *Physics of Solitons* (Cambridge University Press, Cambridge, 2006).

[4] J. Rubinstein, J. Math. Phys. **11**, 258 (1970).

[5] M. J. Ablowitz, D. J. Kaup, A. C. Newell, and H. Segur, Phys. Rev. Lett. **30**, 1262 (1973).

[6] R. Hirota, J. Math. Phys. **14**, 805 (1973).

[7] J. Weiss, J. Math. Phys. **25**, 2226 (1984).

[8] F. M. Russell, Y. Zolotaryuk, J. C. Eilbeck, and T. Dauxois, Phys. Rev. B **55**, 6304 (1997).

[9] O. M. Braun and Y. S. Kivshar, Phys. Rev. B **43**, 1060 (1991).

[10] L. Slepyan, A. Cherkaev, and E. Cherkaev, J. Mech. Phys. Solids **53**, 407 (2005).

[11] S. Flach and A. V. Gorbach, Phys. Rep. **467**, 1 (2008).

[12] S. Sen, J. Hong, J. Bang, E. Avalos, and R. Doney, Phys. Rep. **462**, 21 (2008).

[13] G. Theocharis, N. Boechler, and C. Daraio, in *Acoustic Metamaterials and Phononic Crystals*, edited by P. A. Deymier, Springer Series in Solid-State Sciences (Springer, Berlin, Heidelberg, 2013), pp. 217–251.

[14] N. Nadkarni, C. Daraio, and D. M. Kochmann, Phys. Rev. E **90**, 023204 (2014).

[15] M. B. Fogel, S. E. Trullinger, A. R. Bishop, and J. A. Krumhansl, Phys. Rev. B **15**, 1578 (1977).

[16] P. J. Pascual and L. Vázquez, Phys. Rev. B **32**, 8305 (1985).

[17] P. Biller and F. Petruccione, Phys. Rev. B **41**, 2139 (1990).

[18] S. A. Gredeskul, Y. S. Kivshar, L. K. Maslov, A. Sánchez, and L. Vázquez, Phys. Rev. A **45**, 8867 (1992).

[19] Z. Fei, Y. S. Kivshar, and L. Vázquez, Phys. Rev. A **45**, 6019 (1992).

[20] M. J. Rodriguez-Plaza and L. Vázquez, Phys. Rev. B **41**, 11437 (1990).

[21] V. V. Konotop, A. Sánchez, and L. Vázquez, Phys. Rev. B **44**, 2554 (1991).

[22] A. Sánchez, L. Vázquez, and V. V. Konotop, Phys. Rev. A **44**, 1086 (1991).

[23] Z. Fei, V. V. Konotop, M. Peyrard, and L. Vázquez, Phys. Rev. E **48**, 548 (1993).

[24] V. F. Nesterenko, *Dynamics of Heterogeneous Materials* (Springer, New York, 2001), pp. 65–81.

[25] V. F. Nesterenko, C. Daraio, E. B. Herbold, and S. Jin, Phys. Rev. Lett. **95**, 158702 (2005).

[26] C. Daraio, V. F. Nesterenko, E. B. Herbold, and S. Jin, Phys. Rev. Lett. **96**, 058002 (2006).

[27] C. Daraio, V. F. Nesterenko, E. B. Herbold, and S. Jin, Phys. Rev. E **73**, 026610 (2006).

[28] M. A. Porter, C. Daraio, I. Szelengowicz, E. B. Herbold, and P. G. Kevrekidis, Phys. D **238**, 666 (2009).

[29] F. Li, L. Zhao, Z. Tian, L. Yu, and J. Yang, Smart Mater. Struct. **22**, 035016 (2013).

[30] R. Potekin, K. R. Jayaprakash, D. M. McFarland, K. Remick, L. A. Bergman, and A. F. Vakakis, Exp. Mech. **53**, 861 (2013).

[31] K. Li, P. Rizzo, and X. Ni, J. Appl. Mech. **81**, 071011 (2014).

[32] J. Yang, M. Gonzalez, E. Kim, C. Agbasi, and M. Sutton, Exp. Mech. **54**, 1043 (2014).

[33] A. C. Scott, Am. J. Phys. **37**, 52 (1969).

[34] M. Molerón, A. Leonard, and C. Daraio, J. Appl. Phys. **115**, 184901 (2014).

[35] A. F. Arrieta, I. K. Kuder, T. Waeber, and P. Ermanni, Compos. Sci. Technol. **97**, 12 (2014).

[36] S. A. Emam and D. J. Inman, Appl. Mech. Rev. **67**, 060803 (2015).

[37] N. Nadkarni, A. F. Arrieta, C. Chong, D. M. Kochmann, and C. Daraio, Phys. Rev. Lett. **116**, 244501 (2016).

[38] M. Hwang and A. F. Arrieta, Sci. Rep. **8**, 3630 (2018).

[39] J. R. Raney, N. Nadkarni, C. Daraio, D. M. Kochmann, J. A. Lewis, and K. Bertoldi, Proc. Natl. Acad. Sci. USA **113**, 9722 (2016).

[40] See Supplemental Material at http://link.aps.org/supplemental/10.1103/PhysRevE.98.042205 for term by term projection of Eq. (11) onto ϕ_b. Video S1 shows complete motion in the periodic lattice; video S2 shows complete motion in the lattice with decreasing intersite stiffness; video S3 shows complete motion in the lattice with increasing intersite stiffness; video S4 shows internally excited motion in the lattice with increasing intersite stiffness; video S5 shows complete motion in the lattice with decreasing on-site stiffness; video S6 shows complete motion in the lattice with increasing on-site stiffness; video S7 for internally excited motion in the lattice with increasing on-site stiffness.

[41] A. Chopra, *Dynamics of Structures: Theory and Applications to Earthquake Engineering* (Prentice-Hall, New York, 2012), pp. 683–686.